A Radial Structure Tensor and Its Use for Shape-Encoding Medical Visualization of Tubular and Nodular Structures

Rafael Wiemker, Tobias Klinder, Martin Bergtholdt, Kirsten Meetz,
Ingwer C. Carlsen, and Thomas Bülow

Abstract—The concept of curvature and shape-based rendering is beneficial for medical visualization of CT and MRI image volumes. Color-coding of local shape properties derived from the analysis of the local Hessian can implicitly highlight tubular structures such as vessels and airways, and guide the attention to potentially malignant nodular structures such as tumors, enlarged lymph nodes, or aneurysms. For some clinical applications, however, the evaluation of the Hessian matrix does not yield satisfactory renderings, in particular for hollow structures such as airways, and densely embedded low contrast structures such as lymph nodes. Therefore, as a complement to Hessian-based shape-encoding rendering, this paper introduces a combination of an efficient sparse radial gradient sampling scheme in conjunction with a novel representation, the *radial structure tensor (RST)*. As an extension of the well-known *general* structure tensor, which has only positive definite eigenvalues, the *radial* structure tensor correlates position and direction of the gradient vectors in a local neighborhood, and thus yields positive and negative eigenvalues which can be used to discriminate between different shapes. As Hessian-based rendering, also RST-based rendering is ideally suited for GPU implementation. Feedback from clinicians indicates that shape-encoding rendering can be an effective image navigation tool to aid diagnostic workflow and quality assurance.

Index Terms—Curvature-based rendering, shape-based rendering, vessels, airways, lymph nodes, tumors

◆

1 INTRODUCTION

THIS paper investigates the potential of shape-encoding rendering for specific clinical use cases. In this context, we present the *radial structure tensor* (RST) as a novel technique which improves shape-encoding rendering for lymph nodes.

One of the most urgent problems of medical visualization is how to compress the overwhelming 3D data of modern scanners (e.g., CT, MRI, 3D-X-ray, 3D-US) into 2D overview renderings such that salient points can be grasped quickly under the time pressure of the clinical workflow. It is noteworthy, that in the last decade the data output of medical scanning devices has risen much faster than the computer power, memory capacities, and memory bandwidth, and last but not least, the reading time of the reviewing physicians. Therefore, all kinds of projections from 3D image volumes onto 2D renderings are of interest, such as maximum and minimum intensity projections (MIP, MinIP), averaging and integrating projections such as Digitally Reconstructed Radiographs (DRR), direct volume renderings (DVR), etc.

The conceptually simplest and also most widely used form of 2D rendering of 3D image volumes is based on opacities derived from image intensities. In other words, the prominence (and optionally the color) with which a certain voxel at position $\mathbf{x}$ in the image volume is presented in the rendering depends on its intensity value $I(\mathbf{x})$. This concept is most natural since for most medical modalities the intensity is directly related to a physical density and can be used to discriminate different tissue types. In order to distinguish between different tissues of the same intensity, also the intensities in a voxel-centric neighborhood around $\mathbf{x}$ can be analyzed [1], [2], [3].

Switching from intensities to first derivatives, edge enhancing rendering concepts [4], [5] exploit the local gradient $\mathbf{g}(\mathbf{x})$. Going another step further, second derivatives can be utilized in order to estimate the local shape [4], [6], [7], [8]. The local shape, in turn, can be used for shape-encoding rendering [9], [10]. In this concept, the prominence and color which a certain voxel of the image volume yields in the rendering depends on the shape of the local structure of which the voxel is a part. This shape is not determined by a discrete segmentation of the image volume into explicit distinct objects; rather, the implicit shape information is derived from second derivatives or curvatures [8]. Although the Hessian as well as the curvature matrix-based techniques is beneficial for many use cases, they have limitations for densely packed and hollow anatomical structures. We will show that for these cases a more costly sampling of gradient vectors in a certain neighborhood is advantageous.

The contribution of this paper is threefold:

- We introduce a local radial gradient sampling scheme which is spatially constrained by an opacity

Fig. 1. Vessels, airways, pulmonary nodules, abdominal and axillary lymph nodes emphasized by shape-encoding rendering.

accumulation similar to direct volume rendering, is superior to the local Hessian for densely packed or thin structures, and is well suited for GPU-implementation.

- We introduce the *radial structure tensor* as a formulation to efficiently represent and analyze the local gradient information.
- We revisit the concept of shape-encoding rendering and present its practical use as a navigational aid for specific clinical use cases.

The paper is organized as follows: In Section 2, we review related work to determine local shape information, and motivate the introduction of a novel technique by pointing out shortcomings of Hessian-based rendering methods for some use cases. In Section 3, we explain the radial sampling scheme and the radial structure tensor and its evaluation in detail, and show results on synthetic images in Section 4. Section 5 is dedicated to clinical images: We discuss the concept of shape-encoding rendering as a navigational aid for medical images, present specific clinical use cases, and discuss feedback from clinicians. Discussion and conclusions are following in Sections 6 and 7.

2   RELATED WORK

2.1   Shape-Encoding Rendering of Medical Images

The concept of encoding shape into opacities and colors (shape encoding rendering) can be beneficial in medical visualization for use cases in which benign and possibly malignant structures cannot be discriminated by their intensities (e.g., X-ray or proton densities in CT and MRI), but only by their shape (Fig. 1). Tumors, lymph nodes, and aneurysms are typically densely surrounded by vessels or parenchymal tissue of the same density, and thus may be occluded in renderings based purely on intensity. This can be mitigated by visual cues based on local shape. Applications have been presented to visualize pulmonary nodules [6], [11], [12], colonic polyps [13], and brain aneurysms in CT [14], and axillary nodules in breast MRI [15].

2.2   Gradient Representation by Structure Tensors

The *radial* structure tensor presented in this paper is a variation of the well-known *general* structure tensor [16],

[17], introduced by Förstner and Gülch [18] and Bigün and Granlund [19]. Significant extensions have been given for nonlinear generalizations [20], for multivalued (e.g., color) images [21], for detection of more complicated patterns [22], and for preserving directional information at edge crossing (e.g., fiber tracking) [23].

2.3   Vessel Enhancement

Although the focus of this paper is on enhancing blob-like shapes, vessel enhancing techniques are closely related. Moreover, for the medical applications which we will present, the tubular enhancement can serve as useful anatomical context for the nodular enhancement, making it easier for the user to quickly focus on structures of interest while disregarding others. Furthermore, in order to reflect the continuous transition from tubular to nodular structures in an unbiased way, it is desirable to use the same formulation for both.

A large number of techniques have been published on vessel enhancement in medical images, using—in rough historical order—second derivatives [24], [25], [26], [27], [28], [29], first derivatives [30], [31] as well as direct intensities [32], [33]. Broadly, vessel enhancement techniques can be divided into approaches based on the differential properties of a central point only versus approaches which analyze a certain neighborhood around each voxel, and are superior but significantly more costly. This additional cost is seen as a major limitation for practical use (e.g., 4h for a $100 \times 100 \times 256$ voxel image volume [33]).

For our purpose of enhancing lymph nodes in medical images, we were looking for a voxel-wise technique which lends itself for convenient parallel implementation on a GPU. The approach of Agam et al. [31] as a first step computes a 3D vector field from the scalar image volume (by sampling the neighboring gradients and estimating a principal direction). This means that the memory required on a GPU would at least quadruple (in comparison to the original image volume), even more if float-valued vectors are derived from a typical 16-bit image volume. For larger data sets, this memory requirement poses a serious obstacle.

The method presented in this paper can be seen as a 3D extension of the concept of Pock et al. [30]. The first step of their approach estimates the local orientation by the eigenvectors of the local Hessian. In the second step, they

sample the gradient vectors in a 2D plane perpendicular to the local orientation. Pock et al. [30] employ two different scale spaces for the computation of the Hessian eigenvectors and the gradient sampling. Again, this poses a challenge for GPU implementation as it requires either both scale space representations to be held in memory simultaneously, or—even costlier—a vector field stored additional to the image volume. In contrast, we strive to present a method which samples the gradients in a 3D neighborhood around each voxel, works on a single scale space level, and uses sparse radial sampling to avoid exceeding computation costs (Section 3).

2.4 Hessian-Based Rendering

We would like to review two shape encoding rendering techniques which both utilize the local Hessian matrix. Hessian-based methods are the historically first, the simplest, and the most widely known methods to estimate local shape. The first technique maps the second derivatives directly onto color intensities, whereas the second technique uses the Hessian in conjunction with the local gradient vector to estimate the local curvature of the implicit isointensity surface, and then maps the curvature eigenvalues onto color intensities.

2.4.1 Second-Derivative-Based Rendering

For Hessian-based rendering [6], [11], the second spatial derivatives are computed at a position $\mathbf{x}$ and assembled into the 3×3 Hessian matrix $\mathrm{H}(\mathbf{x})$ as $H_{ij} = \partial^2 I / \partial x_i \partial x_j$ with $i, j \in \{x, y, z\}$. In practice, the spatial derivatives are computed as finite differences in a very small neighborhood, after the original image volume is prefiltered with a Gaussian smoothing filter of a certain scale resolution. The resolution scale can either be fixed for a certain structure size, or the maximum response can be selected from a range of resolution scales [34], [35]. The Hessian is symmetric, and thus an eigenvalue decomposition yields three real positive or negative eigenvalues which are ordered by magnitude $|\lambda_0| \geq |\lambda_1| \geq |\lambda_2|$. The eigenvalue decomposition can be computed either iteratively or using the trigonometric closed-form solution of the characteristic cubic equation.

A very simple but surprisingly effective rendering scheme just maps the two weaker eigenvalues λ_1 and λ_2 directly onto color intensities:

$$
\begin{aligned}
-\mathrm{I}_{\mathrm{Red}} &\propto |\lambda_1| \text{ if } \lambda_0 \leq \lambda_1 < 0 & \text{`vesselness'} & \quad V \\
-\mathrm{I}_{\mathrm{Blue}} &\propto |\lambda_1| \text{ if } \lambda_0 \geq \lambda_1 > 0 & \text{`airwayness'} & \quad A \quad (1) \\
-\mathrm{I}_{\mathrm{Yellow}} &\propto |\lambda_2| \text{ if } \lambda_0 \leq \lambda_1 \leq \lambda_2 < 0 & \text{`blobness'} & \quad B.
\end{aligned}
$$

Each of these features is subjected to an individual maximum projection, and finally composed into a combined MIP [6], [11], [12] (Fig. 1, and more clinical examples in Section 5). Note that (1) implies that a voxel with nonvanishing blobness will always also exhibit at least the same amount of vesselness; this is unproblematic as it yields a mixed yellow/red color for blob-like structures which is distinct from the pure vesselness color red.

Alternatively to (1), in the Experiments-section, we also use the following eigenvalue combination as suggested by Li et al. [25]:
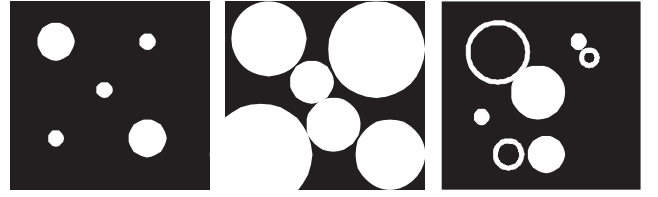

Fig. 2. Example constellations where Hessian-based rendering works well (left) and where it does not suffice: densely packed (middle), and hollow structures (right).

$$
\begin{aligned}
\text{`vesselness'} & \quad V \propto |\lambda_1|(|\lambda_1| - |\lambda_2|)/|\lambda_0| \text{ if } \lambda_0 \leq \lambda_1 < 0 \\
\text{`airwayness'} & \quad A \propto |\lambda_1|(|\lambda_1| - |\lambda_2|)/|\lambda_0| \text{ if } \lambda_0 \geq \lambda_1 > 0 \\
\text{`blobness'} & \quad B \propto |\lambda_2|^2/|\lambda_0| \qquad \text{if } \lambda_0 \leq \lambda_1 \leq \lambda_2 < 0.
\end{aligned}
\quad (2)
$$

2.4.2 Curvature-Based Rendering

Curvature of the implicitly given isointensity surface is closely related but not identical to the second derivatives. Kindlmann et al. [8] have summarized how the two curvature eigenvalues can be extracted very efficiently in closed form from the Hessian matrix and gradient vector. These can be mapped on color intensities in a similar fashion as described above, and yield very similar renderings as the directly Hessian-based methods.

2.5 Limitations of Hessian-Based Methods

All Hessian-based techniques rely on the assumption that the local shape can be estimated sufficiently by the local Hessian $\mathbf{H}(\mathbf{x})$ and optionally the local gradient $\mathbf{g}(\mathbf{x})$ computed only at the central position $\mathbf{x}$. The underlying idea is that the information contained in the surrounding neighborhood $N(\mathbf{x})$ is collected by the prior convolution of the image volume with a Gaussian filter of scale σ. However, for certain applications (Fig. 2) this may not suffice, in particular for the case of

- densely packed structures (e.g., abdominal lymph nodes), where the typical distance between several structures is smaller than their extent, and a large-scale smoothing would blend unrelated structures into each other,
- hollow structures (e.g., airways), where the defining wall is thin in comparison to the structure size. To get a Hessian filter response for the structure, a large smoothing scale is required, which in turn wipes out the thin wall.

In Section 4, we will show simulation phantoms which demonstrate that the Hessian eigenvalues, and thus also filters derived from those such as the Li-filter [25], fail to respond properly to nodules with other structures too closely adjacent.

3 APPROACH

In order to overcome the limitations of extracting the shape from the local Hessian $\mathbf{H}(\mathbf{x})$ and the gradient $\mathbf{g}(\mathbf{x})$ solely at point $\mathbf{x}$, we consider sampling the gradient $\mathbf{g}$ in a certain neighborhood of radius R around $\mathbf{x}$. The underlying idea is that the sampling of neighboring gradients and the analysis
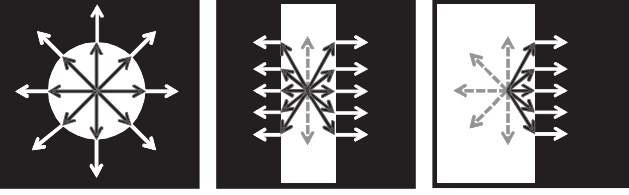
Fig. 3. Central cross sections through a 3D sphere, cylinder, and step-edge, yielding, respectively, a high 3D correlation (left), 2D correlation (middle), and low correlation (right) between gradient vectors and radial vectors.

of their behavior with respect to their relative location can yield more information than the second derivative evaluated at one location of a coarse scale space level only. Our aim is to sample gradients at a scale space resolution which is significantly smaller than the structure size, and not compromised by excessive smoothing.

3.1 Sparse Radial Gradient Sampling Scheme

In principle, the local shape can be established by sampling the intensities $I(\mathbf{x}')$ and gradient vectors $\mathbf{g}(\mathbf{x}')$ for all points $\mathbf{x}'$ within a certain radius R around $\mathbf{x}$. (For the standard Hessian approach, this is achieved by a prior convolution of the image volume with a Gaussian.) However, the full sampling of all gradients in a spherical neighborhood around each point $\mathbf{x}$ poses two problems:

- The sampling cost becomes very high for nonsmall structures as the number of points to be sampled increases with the third power of the radius R. (This known cost problem of voxel-centric neighborhood sampling is also discussed in [1], [2], [33]).
- The indiscriminative sampling of all gradients in a spherical neighborhood may mix information from the central structure with other adjacent but unrelated structures.

In order to mitigate both problems at once, we suggest to use a sparse radial sampling ray casting scheme (Fig. 3) along a number of N_R isotropically distributed search rays cast out from the center voxel $\mathbf{x}$. The basic idea is to follow these rays in the same fashion as along the view rays in standard direct volume rendering.

Use of this radial sampling scheme achieves two main advantages: First, the effort increases only linearly with the maximum sampling radius R, because the number of rays N_R and the step size Δr are fixed. Although this is paid for with a quadratic loss of accuracy with increasing radius and risk of undersampling artifacts, it allows near interactive computation times. Second, we use a technique inspired by direct volume rendering [36] in order to avoid leaving the local structure of interest and penetrating an adjacent structure: Along each search ray, we accumulate an increasing opacity $\alpha(d(\mathbf{x}')) \in [0..1]$ which is based on the intensity difference $d = |I(\mathbf{x}') - I(\mathbf{x})|$ between the central value $I(\mathbf{x})$ and the intensity $I(\mathbf{x}')$ at search ray position $\mathbf{x}'$. Let us separate each search ray into a variable length and the constant normalized radial direction: $\mathbf{r} = r \cdot \hat{\mathbf{r}}$. Let us further parameterize the radial rays with index i and the steps along each ray with index k, so that $\mathbf{x}'_{ik} = \mathbf{x} + k\Delta r \cdot \hat{\mathbf{r}}_i$, where $\hat{\mathbf{r}}$ is the normalized radial direction of the search ray.

Then, the increasing opacity α_{ik}, which starts with 0 at $k = 0$ for each ray $\hat{\mathbf{r}}_i$, becomes a function of k.

Once the accumulated opacity approaches 1, the ray i can be terminated. The desired effect is that no further gradients are sampled outside the structure of interest. This scheme avoids usage of a hard threshold, and is known from standard volume rendering [36] to yield good results also in the presence of noise. The monotonously increasing opacity α is accumulated from incremental local opacities $\Delta\alpha$ given by an opacity transfer function (TF) $f(d)$ which increases with the intensity difference $d = |I(\mathbf{x}') - I(\mathbf{x})|$ between local intensity at $\mathbf{x}'$ and intensity at the ray casting origin $\mathbf{x}$. The opacity transfer function f can be any monotonous continuous function, but for simplicity we use a piecewise linear function $f(d)$ with

$$f(d) = \begin{cases} 0 & \text{if } d \leq d_{\min} \\ (d - d_{\min})/(d_{\max} - d_{\min}) & \text{if } d_{\min} < d < d_{\max} \\ 1 & \text{if } d \geq d_{\max} \end{cases} \quad (3)$$

with application-dependent parameters d_{min} and d_{max}.

Sampling in fixed steps of length Δr along the search ray, the opacity at the ith step is updated from the previous step as

$$\alpha_i = \alpha_{i-1} + (1 - \alpha_{i-1})f(d_i)\Delta r. \quad (4)$$

Along the ray, the local gradients $\mathbf{g}(\mathbf{x}') \hat{=} \mathbf{g}_{ik}$ are sampled and weighted with the local opacity $\alpha(d(\mathbf{x}')) \hat{=} \alpha_{ik}$. Each ray is terminated if either the radius becomes larger than a certain maximum radius R or if the opacity α approaches 1.

3.2 The Radial Structure Tensor

The concept of combining all sampled gradients in a neighborhood is well known from the structure tensor $\mathbf{S}$ [16], [17], [18], [19]. The structure tensor is constructed by summing up the outer product of the gradient vectors $\mathbf{g}(\mathbf{x}')$ for all points $\mathbf{x}' \in N(\mathbf{x})$, weighted usually by a Gaussian term of the distance $d(\mathbf{x}')$ to the central point $\mathbf{x}$:

$$\mathbf{S} = \sum_{\mathbf{x}' \in N(\mathbf{x})} \mathbf{g} \cdot \mathbf{g}^T \cdot G(d(\mathbf{x}')). \quad (5)$$

Then, the symmetric positive definite structure tensor is analyzed by virtue of its three real nonnegative eigenvalues. This *general* structure tensor, however, is not very discriminative for nodular and tubular structures, as it collects all gradient vectors $\mathbf{g}(\mathbf{x}')$ regardless of their position $\mathbf{x}'$. In particular, it does by construction (5) not distinguish between gradients pointing inwards or outwards with respect to the center position $\mathbf{x}$ (Fig. 3).

To achieve a higher discriminative power for nodular structures, we therefore introduce the *radial structure tensor*, which we construct as

$$\mathbf{T} = \sum_{\mathbf{x}' \in N(\mathbf{x})} \hat{\mathbf{g}} \cdot \hat{\mathbf{r}}^T \cdot g, \quad (6)$$

which sums up the outer vector product of the normalized vectors $\hat{\mathbf{g}}$ and $\hat{\mathbf{r}}$ weighted with the gradient magnitude $g = |\mathbf{g}|$.

We write the radial vector $\mathbf{r} = (\mathbf{x} - \mathbf{x}')$ which is pointing from the center position $\mathbf{x}$ to the gradient vector location $\mathbf{x}'$
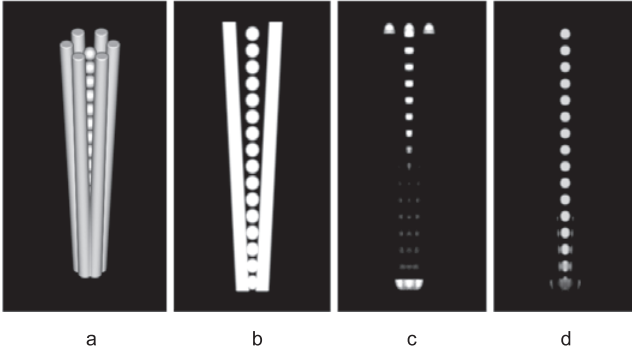
Fig. 4. (a) Direct volume rendering of a 3D simulation phantom with a string of spheres (nodules) surrounded by cylinders (vessels). (b) Central slice of the phantom. (c) Response of the third eigenvalues of the Hessian, after a Gaussian convolution with an optimal filter width (equal to the radius of the spheres). (d) Response of the third eigenvalues of the radial structure tensor. Using the Hessian (c), the filter response of the spheres is clearly distorted due to the close adjacency between the spheres. Moreover, below a certain closeness of the adjacent vessels, the response of the spheres vanishes. Both problems are overcome by the radial structure tensor (d).
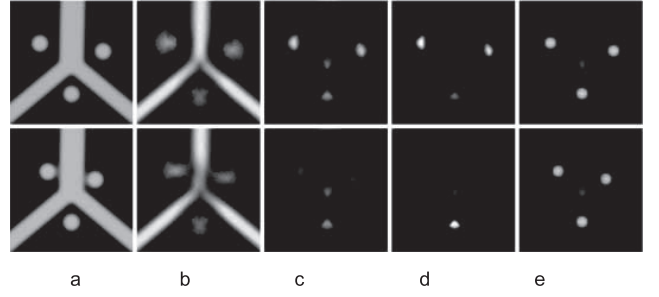

Fig. 5. Top row: 3D Simulation phantom with three nodules close to a vessel bifurcation. Bottom row: Similar phantom, with nodules closer to vessel. (a) Central slice. (b) Response of the second eigenvalue of the Hessian. (c) Response of the third Hessian eigenvalue. (d) Response of the Li-blobness-filter. (e) Response of the third eigenvalues of the radial structure tensor (RST). In the second phantom (bottom row) with closer adjacencies, the responses of the second and third Hessian eigenvalue are clearly compromised by the adjacent structures, thus leading to the vanishing of two nodules and severe distortion of the third nodule in the Li-blobness-filter [25] (d). The RST-approach (e) is not affected by the close adjacencies.

as the product of length and normalized direction $\mathbf{r} = r \cdot \hat{\mathbf{r}}$, and in the same way the gradient vector $\mathbf{g} = g \cdot \hat{\mathbf{g}}$.

Thus, the tensor $\mathbf{T}$ captures the covariance between the normalized radial vectors $\hat{\mathbf{r}}(\mathbf{x}')$ and the gradient vectors $\mathbf{g}(\mathbf{x}')$; or in other words, the covariance between the radial direction $\hat{\mathbf{r}}$ and the normalized gradient direction $\hat{\mathbf{g}}$ weighted with the gradient magnitude g. The motivation for the construction of the radial structure tensor is the following.

For ideal spherical objects, the radial vectors $\hat{\mathbf{r}}$ should be in total correlation with the gradient directions $\hat{\mathbf{g}}$ on their surface (Fig. 3). The positive or negative sign of the correlation indicates whether it is a bright object on dark background or vice versa. For cylindrical objects, we expect a correlation of directions along two principal axes, but vanishing direction in the third. For sheet-like structures, we expect correlation of gradient and radial directions in only one principal axis. Neighborhoods with gradient vectors pointing into arbitrary directions may show significant entries of the general structure tensor $\mathbf{S}$, but vanishing entries of the radial structure tensor $\mathbf{T}$ since the gradient directions $\hat{\mathbf{g}}$ do not correlate with their positions relative to the center point $\mathbf{x}$.

Using the radial ray casting sampling scheme (Section 4.1), we replace the integration over all positions $\mathbf{x}'$ by the summation over all radial rays i with the finite radial steps indexed by k. Additionally, all gradient magnitudes g_k sampled along the search rays are weighted with the respective opacities α_k along the ray:

$$\mathbf{T} = \sum_{i,k} \alpha_{ik} \cdot g_{ik} \cdot \hat{\mathbf{g}}_{ik} \cdot \hat{\mathbf{r}}_i^T = \sum_{i,k} \alpha_{ik} \cdot \mathbf{g}_{ik} \cdot \hat{\mathbf{r}}_i^T \qquad (7)$$

with $\hat{\mathbf{r}}$ and $\hat{\mathbf{g}}$ the normalized radial and gradient vectors, and α, $\mathbf{r}$, and $\mathbf{g}$ all evaluated at each ray position $\mathbf{x}'_{ik} = \mathbf{x} + k\Delta r \cdot \hat{\mathbf{r}}_i$.

The 3×3 matrix $\mathbf{T}$ is generally not symmetric. It would be symmetric only for a point-symmetric image neighborhood around $\mathbf{x}$. For the purpose of describing the local shape as point-symmetric archetypes such as cylinders, spheres, and sheets, we are not interested in local image asymmetries, and thus choose to symmetrize the structure tensor by adding the transposed matrix as $\mathbf{T}_s = \mathbf{T} + \mathbf{T}^T$. This guarantees that its three eigenvalues are real. The symmetrized tensor yields three significant correlation eigenvalues for spherical objects (e.g., lymph nodes), two significant and one vanishing eigenvalue for cylindrical objects (e.g., vessels or airways), one significant and two vanishing eigenvalues for sheet-like objects, and nonsignificant correlation eigenvalues otherwise.

Unlike the normal structure tensor, which is positive definite, the eigenvalues of the radial structure tensor can be positive or negative and can be used for the derivation of vesselness, airwayness, and blobness features [25] in the same way as the eigenvalues of the Hessian matrix (1). Similar to Hessian-based rendering, the tensor eigenvalues or derived features can be mapped onto colors and displayed as maximum intensity projections (Fig. 7).

4 EXPERIMENTS

Simulated 3D phantom data sets have been used to validate the correctness of the combined radial ray sampling and RST representation. The superiority of the RST based over the Hessian-based approach is demonstrated in Figs. 4 and 5 with respect to densely adjacent structures. Fig. 6 demonstrates the superiority of the newly introduced *radial* structure tensor over the *general* structure tensor (6d), and shows superiority over the Hessian approach with respect to smaller response at bifurcations (Figs. 6e, 6f, and 7). More comparisons figures on true medical data will be presented in Section 5.

4.1 Distribution of Search Rays

The number N_R of search rays determines the specificity and noise robustness of the enhancement (see next section), but will increase computation costs in a linear way. An isotropic distribution of the search rays is desirable, but in practice an approximation will suffice; a pragmatic scheme is given in [37]. The effect of a not ideally isotropic ray distribution is negligible in comparison to the anisotropy inherent in the data itself (CT data are typically reconstructed with anisotropic voxel spacing and the physical resolution is location dependent). We have tested several
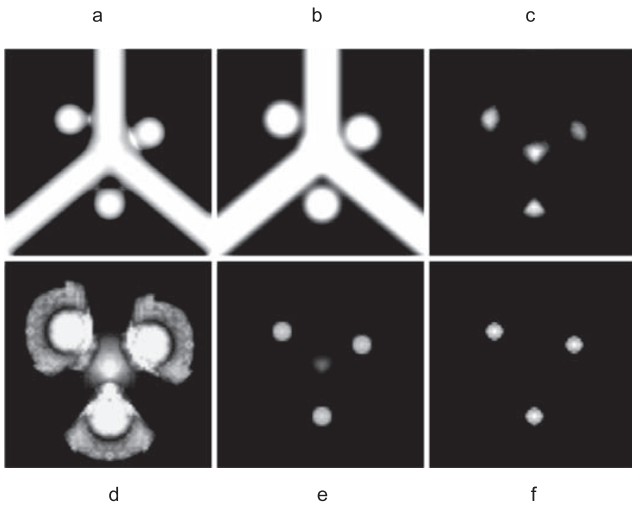
Fig. 6. Three-dimensional simulation phantom with three nodules close to a vessel bifurcation. (a) Direct volume rendering. (b) Central slice. (c) Response of the third Hessian eigenvalue. (d) Response of the third eigenvalue of the standard structure tensor. (e) Response of the third eigenvalue of the radial structure tensor. (f) RST response after subtraction of bifurcation response. The standard structure tensor (d) is not sufficiently discriminative as it does not correlate gradients with locations. The third RST eigenvalues responds clearly weaker to bifurcations than the third Hessian eigenvalues. The magnitude of the bifurcation response can thus be subtracted from the overall image without compromising the nodule responses.

different approximating schemes: the normals of the faces after one subdivision of an icosahedron (42 rays), and the vectors to the face centers of a $k \times k \times k$ cube with $k = 3, 5, 7$ yielding $N_R = 26, 98, 218, 386$ rays.

4.2 Noise Properties

The filter response of the radial sampling in conjunction with the RST decreases with increasing noise, due to two sources of error:

1. The estimation of the local gradient vectors becomes unreliable.
2. The radial search rays are terminated prematurely by noisy voxels along their way.

We have simulated the decrease of the blobness filter response with increasing noise for synthetic but realistic data of a typical 10 mm lymph node (Fig. 8).

The opacity transfer function used to build up the opacity along the ray should be adjusted to the image noise
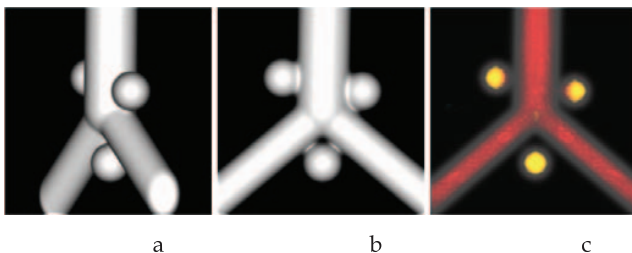

Fig. 7. Three-dimensional simulation phantom with three nodules close to a thicker vessel bifurcating into two thinner vessels. (a) Direct volume rendering, showing the slight bulge at the bifurcation. (b) Direct volume rendering, frontal view. (c) Color-coded composite MIP of original intensity (gray), second (red), and third (yellow) eigenvalues of the radial structure tensor, showing only a small response at the bifurcation.
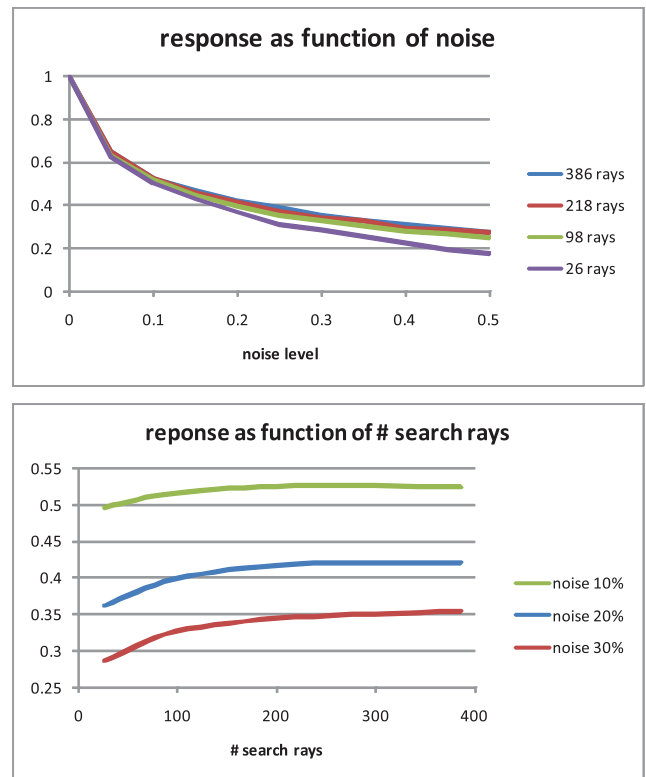

Fig. 8. The ordinates show the relative response of the blobness feature (1.0 for the noise-free case) as a function of noise (top) and as a function of the number of search rays (bottom), measured on a synthetic 10 mm sphere (typical lymph node size) with 0.5 mm voxel spacing (typical CT scan), a typical contrast of 100 Hounsfield units (HU) between node and surrounding tissue, and Gaussian noise with a standard deviation $\sigma = [0...50\mathrm{HU}]$ (i.e., $\sigma = [0...0.5]$ relative to the contrast), using 1,000 simulations per data point.

level such that a ray terminates at the boundary of the object of interest but not by intensity variation within the noise level. There are many ways to design appropriate TFs with respect to image noise and object contrast, just as in standard volume rendering [38]. We have conducted the simulations with a linear TF as in (3) with $d_{\min} = 0$ and reaching saturation at $d_{\max} = 2\sigma$.

The problem of noise corrupted gradients (error source 1) can be mitigated by simply increasing the number of search rays N_R. However, the premature ray termination (error source 2) persists even for a higher number of search rays, so that we do not observe improvement above $N_R = 200$ rays for our synthetic test case (Fig. 8). So, the number of rays N_R can be chosen either to optimize the performance for a given image noise level, or as a compromise between computation time and performance.

4.3 Implementation Issues and Computation Time

Since all voxels of the image volume are treated independently and on equal footing, the radial gradient sampling and eigenvalue decomposition of the radial structure tensor are ideally suited for parallel processing on a GPU. For the implementation, it makes sense to divide the algorithm into a one-time feature-computation phase, and an interactive maximum projection of the precomputed features. This requires that additionally to the original image volume one volume for each feature (vesselness, blobness, airwayness,
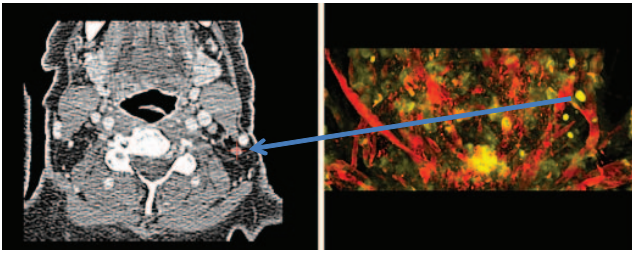
Fig. 9. Image navigation by mouse click on the lymph node enhancing rendering, leading to the appropriate position in the standard slicewise display of the CT data set of the neck. Left: axial slice. Right: coronal maximum projection of radial structure tensor eigenvalues.

Fig. 10. CT volume of axillary region. Standard intensity MIP (gray), overlayed with noduleness response only (yellow), and composite of intensity, noduleness, and vesselness (red), providing improved context information and perception.

original positions, etc.) is allocated on the GPU. Conveniently, these feature volumes never have to be transferred back to the CPU memory space. For the eigenvalue decomposition, we use the trigonometric closed-form solution of the characteristic cubic equation. For a CT data sets with $512 \times 512 \times 541$ voxels (using 42 search rays per voxel with a maximal range of 15 mm, and $d_{\min} = 10$, $d_{\max} = 30$ for the TF (3)), we observe typical feature computation times of ca. 20 seconds using a nonoptimized CUDA implementation on a NVIDIA Quadro 5000, in comparison to ca. 5 seconds for computation of the Hessian eigenvalues. The spatial derivatives are computed as finite differences after prior Gaussian smoothing. Along the rays, we used trilinear interpolation between the data grid positions (as implicitly provided by the CUDA environment).

5 CLINICAL APPLICATIONS

5.1 Shape-Encoding Visualization as a Navigational Aid for Medical Applications

Shape-encoding rendering is a known visualization concept, but it has not yet reached wider use in clinical practice. Our proposition is that its clinical benefit may lay less in diagnostic appraisal of the rendering itself, but more in its usage as a navigational aid to high-dimensional image data.

If—for a specific clinical use case—a shape-encoding rendering succeeds in bringing suspicious shapes prominently into the visual foreground, then it may be helpful for

- effective navigation through 3D volumes,
- quick diagnostic appraisal (screening workflow),
- help against oversights (diagnostic quality assurance).

To become a clinically useful tool, it is essential that the rendering does not replace the conventional slicewise display of the original unprojected volume data. Rather, each point in the rendering must be related to the 3D location where it originated from, so that the clinician can quickly inspect the appropriate slice location in the conventional slicewise display (Fig. 9).

The concept of shape encoding can be applied to direct volume renderings (Fig. 12) as well as to maximum intensity projections (MIPs, all other figures). Both projection types have advantages and disadvantages with regard to specific clinical use cases, and their comparative efficiencies have to be assessed in multireader studies for sp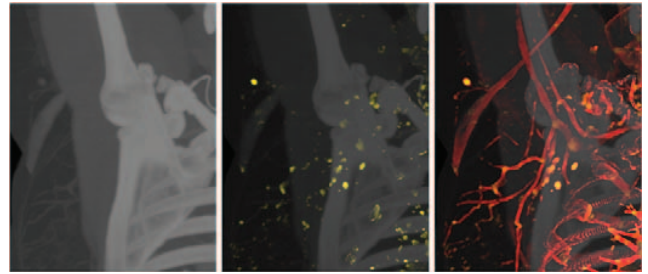ecific clinical use cases [39]. Direct volume renderings have, as their main advantage, the good impression of depth and spatial context they convey to the user. Therefore, they are beneficial, e.g., for surgical applications and for close inspection of points of interest which have already been singled out. For diagnostic overview, however, their main disadvantage is the possible occlusion of structures. Maximum projections on the other hand guarantee to always bring salient features to the foreground. By construction, MIPs do not convey depth cues, but an intuitive depth impression can be provided simply by allowing the user to interactively rotate the rendering. Even though maximum projections often appear more cluttered and prone to noise than direct volume renderings, they may be more effective for early diagnostic overview, and be more trusted by clinicians because of their lower risk of occlusion of salient structures. Therefore, in this paper, we concentrate on shape-encoding rendering using maximum projections rather than volume renderings.

5.2 Compositing of Multiple Color-Coded Shape Types

Computer-aided detection (CADe) systems essentially compute a sophisticated abnormality likelihood for each pixel and display a discrete marker if the likelihood exceeds a certain threshold [40], [41]. In an alternative, nonbinary but gradual visualization mode, the abnormality likelihood can be shown as an unthresholded continuous color overlay. A typical problem is the presence of irrelevant responses, e.g., strong bendings or bifurcations of vessels giving blob-like responses. This problem is inherent, as the transition between a thickening in a vessel and a vascularized nodule is a gradual one, which cannot be partitioned by a clear rule. Therefore, it is advantageous to show vesselness and blobness responses to the reader at the same time, differentiated only by color (for comparison see Fig. 10). The context information given by the compositing of various filter responses aids the perception such that the reader can quickly learn which combination of responses may be of interest for further inspection and which to ignore. The physician may trust such a color-coded multienhancing composite visualization more than an automated suppression of false positives by a black-box CADe system.

5.3 Clinical Use Cases

We have identified several specific use cases in the clinical routine where shape-encoding rendering could be helpful. A clinical evaluation follows in the next section.

Fig. 12. A direct volume rendering (instead of a maximum intensity projection), with colors derived from Hessian eigenvalues.
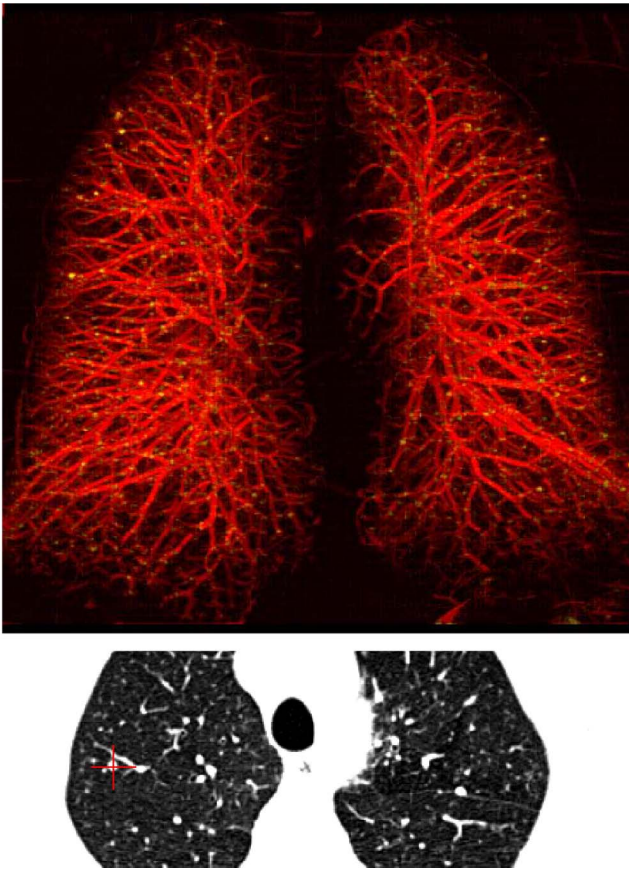
Fig. 11. Top: Hessian eigenvalues-based rendering; superposition of MIPs of second and third eigenvalue (reddish and yellowish, respectively). The lung shows a number of minuscule nodules (one example marked in the axial slice view, bottom) which can be easily overlooked in the standard slicewise viewing but are emphasized as yellow dots in the rendering. Due to the context provided by the reddish vessel responses, the mind of the clinical user can learn quickly to disregard the responses at vessel bifurcations.

5.3.1 Pulmonary Nodules

Lung cancer screening using regular CT examinations has very recently been shown to have the potential to reduce mortality by 20 percent or more [42]. Although, small pulmonary nodules are mostly benign, their detection and appraisal is a clinical routine task, since they can possibly be primary lung cancer tumors or metastases from other cancers. The fact that small nodules can easily be overlooked in the maze of pulmonary vessels has been the reason for the development of computer-aided detection algorithms [40]. Figs. 11, 12, and 13 show that a shape encoding color mapping can emphasize the presence of nodules very effectively, thus reducing the risk of oversight.

5.3.2 Airways

Inspection of the airways on CT images is a routine task for baseline diagnosis and progression monitoring of chronic obstructive respiratory disease (COPD), a disease with constantly rising incidence [43]. The aim of automatic segmentation of the airway tree has motivated a rich field of mostly very sophisticated algorithms (a comparison is given in [44]). In contrast to these explicit segmentation approaches, a nonlabeling voxel-wise rendering may

already be helpful for the diagnostic workflow, at least as an aid for quick navigation. In our experience, the Hessian eigenvalues are only moderately useful for visualization of thinner airways, but the eigenvalues of the radial structure tensor can emphasize the airways in a much more detailed way (Fig. 14).

5.3.3 Lymph Nodes

The detection and appraisal of lymph nodes (typical size 10 mm, typical density similar to water) is a standard task for oncology diagnosis, staging and therapy response monitoring. The finding of the lymph nodes can be quite tedious, e.g., in the cervical, axillary, mediastinal, para-aortic, iliac, femoral, and inguinal areas, where they are
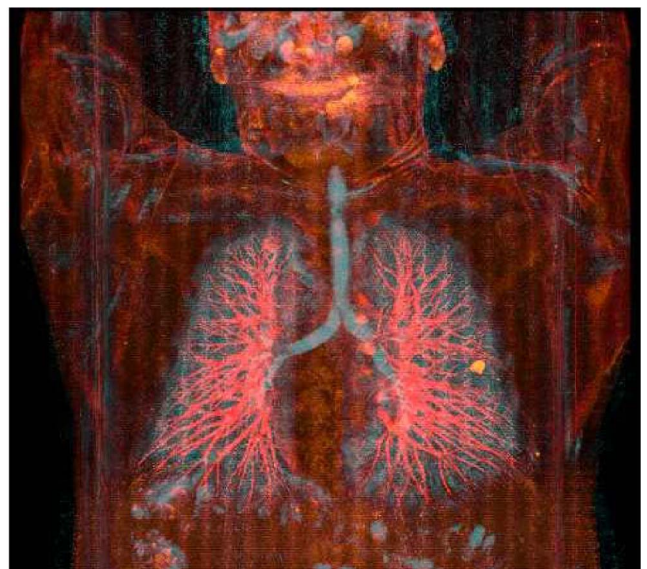

Fig. 13. Patient with a single pulmonary nodule, visible in the shape-encoding rendering of the CT scan, using eigenvalues of the radial structure tensor. Note that with shape encoding no prior segmentation of the lungs is necessarily required.
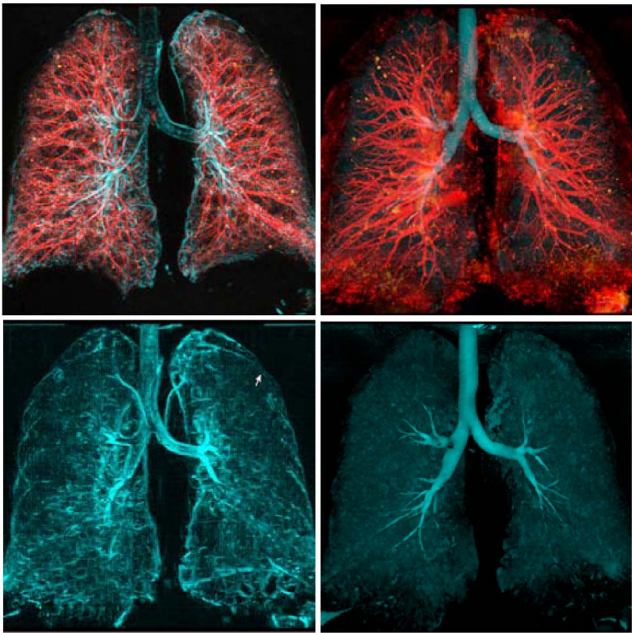
Fig. 14. Comparison between Hessian-based rendering (left) and RST-based rendering (right). Bottom: Response of *airwayness* only. Top: Composite MIPs from *blobness*, *vesselness*, *airwayness*.

densely surrounded by other anatomical structures, in particular vessels, and can be discriminated only by their shape.

5.3.4 Whole Body PET/CT Appraisal

In oncological practice, it is a routine task to check combined PET/CT whole body scans for hot spots which may indicate inflammation or cancerous malignancies. The hot spots arise from FDG accumulation and are visible in the PET scan. The accompanying CT scans are used to analyze which FDG hotspots stem indeed from lymph nodes, and which lymph nodes do not show FDG activity. For this use case, the shape-encoding rendering is applied only to the CT data (due to the comparatively low spatial resolution of the PET). For clinical practice, it is important that the whole body scan can be displayed in one piece (ca. 2,000 slices, high memory and processing demand), and that all three viewports (PET, CT, shape-rendering) are coregistered for manual interaction (Fig. 21).

5.3.5 Vascular Structure

Vessels in all body parts are mostly surrounded by other anatomical structures of equal density, and thus are easily occluded in MIPs or DVRs, in particular in scans without administration of contrast agents such as iodine or gadolinium. Using shape-encoding rendering, appraisal, and search for possible anomalies of the vascular system is feasible without explicit segmentation and suppression of surrounding structures.

5.4 Clinical Evaluation

Since the shape-encoding rendering is used as an image navigation aid and not as a computer-aided detection system, it is not possible to evaluate the performance by counting true and false positives. The suggested rendering is not intended to provide lists of discrete objects on which

to compute statistics. Rather, the suggested shape-encoding rendering is intended as a tool for quality assurance and easing the burden of image reading.

Also, the total reading time for a given case is not necessarily expected to be shortened, as the radiologists are obliged to scrutinize all slice images carefully and look also for incidental findings other than the primary purpose of the scan. Therefore, clinical feedback has been collected by interviews.

5.4.1 Clinical Interviews

Review sessions with Hessian- and RST-based shape-encoding rendering have been conducted with 12 board-certified radiologists at four different university hospitals (see Acknowledgment section) for MRI and CT use cases.

The interviews were conducted in the following way: First, the underlying concept of shape encoding was explained. Second, example cases were shown on a demonstrator software with interactive rendering (GPU-based implementation). Third, a questionnaire was filled out during the interview, and additional comments were collected.

In the interactive demonstrator software, viewing angle, zoom, and slab thickness could be changed continuously, and also the mode of standard versus Hessian- versus RST-based rendering, as well as the respective contributions of the vesselness and blobness features to the color rendering. In order to allow for a wider and more rigorous clinical evaluation, the implementation is planned to be made available as a module of the Philips IMALYTICS Research Workstation (Philips Research, Aachen, Germany).

Five questions (see table and results section below) were given on a questionnaire in a checkbox style on a five-point-scale. Questions 1 and 2 (Overall Usefulness and Hessian versus RST Rendering) were to be answered individually for each of eight clinical use cases (listed in the following section), while questions 3-5 were to be answered in general.

	-2	-1	0	+1	+2
Overall clinical usefulness : (for each specific use case)					
	distracting		neutral		potentially useful
Preferred rendering type: (for each specific use case)					
	Hessian		neutral		RST
Preferred feature encoding:					
	blobness only		neutral		blobness + vesselness
Preferred viewport for shape-encoding rendering:					
	overlayed onto standard port		neutral		separate viewport
Preferred projection type for shape-encoding rendering:					
	MIP		neutral		DVR

5.4.2 Questionnaire Results

Evaluations results are given in a range of $[-2 \cdots +2]$ derived from the five point scale.

Question 1. Overall clinical usefulness of the shape encoding, ordered by preference:

+1.1 whole body lymph node appraisal in PET/CT

+1.0 abdominal lymph nodes

+1.0 cervical lymph nodes in CT

+0.8 axillary lymph nodes in CT

+0.7 axillary lymph nodes in breast MRI
+0.5 lung nodules in CT
+0.1 airway appraisal in CT
0.0 vascular system appraisal in CT

Conclusion. The clear focus of interest for shape-encoding rendering was the appraisal of lymph nodes.

Question 2. Preferred rendering type, ordered by preference (Hessian [−2] versus RST [+2]):

+2.0 airway appraisal in CT
+2.0 whole body lymph node appraisal in PET/CT
+2.0 abdominal lymph nodes
+2.0 cervical lymph nodes in CT
+1.2 axillary lymph nodes in CT
−2.0 axillary lymph nodes in breast MRI
−2.0 lung nodules in CT
−2.0 vascular system appraisal in CT

Conclusion. The opinions were essentially unanimous: Especially lymph nodes were perceived to manifest much more clearly in the RST-based rendering, whereas vessels were favored in the Hessian-based rendering.

Question 3. Feature encoding, blobness only [−2] versus blobness and vesselness [+2]:

Result average. +1.8. Conclusion. Clear preference for color coding of both blobness and vesselness instead of blobness alone, for better spatial orientation.

Question 4. Conventional viewport with overlayed colors [−2] versus additional viewport [+2]:

Result average. +1.5. Conclusion. Preference for additional separate viewport, spatially linked to unchanged standard viewport.

Question 5. Projection type MIP [−2] versus DVR [+2]:

Result average. −2.0. Conclusion. Unanimous preference for MIP over DVR (due to possible occlusions and lack of actual clinical use of DVR).

5.4.3 Anecdotal Evidence

An important result which was not caught by the questionnaires themselves but by direct oral feedback is that the added clinical value was rated moderate or low for dedicated experts of a specific body region, but higher for less experienced staff or readers with another focus of expertise. In other words, for an expert of a specific clinical use case, the standard slicewise gray-scale viewing is perceived as sufficient, while the shape-encoding rendering is expected to give most added value as a safeguard against oversights if the specific clinical question is not a routine task for the reading physician.

Using the additional shape-encoding rendering, all interviewed clinicians have identified additional findings (lymph nodes and nodules) which had escaped their attention on standard gray-scale slicewise viewing and gray-scale MIPs. Moreover, the shape-encoding MIPs were perceived as helpful for the appraisal of the overall spatial constellation.

An example of the power of the shape-encoding rendering is given in Fig. 18, showing a string of minuscule nodes, which in the standard slicewise viewing would easily escape attention.

For high contrast regions such as pulmonary nodules in CT and axillary lymph nodes in breast MRI, the consensus between the interviewed radiologists was that the Hessian-based rendering was sufficient or preferable over the

RST-based rendering. For lymph nodes in anatomically more densely packed body regions, however, Hessian-based rendering was found not to be satisfactory and clearly inferior to RST-based rendering.

The RST-based rendering raised interest in particular for whole-body PET/CT data sets of lymphoma patients (Fig. 21, acquired after injection of ^{18}F-Fluorodeoxyglucose). The shape encoding was applied to the low-dose CT images (30 mAs) acquired for PET attenuation correction purposes, which exhibit a quite noisy image quality. For diagnostic purposes, it has to be analyzed which FDG hotspots in the PET image stem from lymph nodes and which from brown fat, and also which lymph nodes do not show FDG activity. The correctness of the RST-based rendering was verified and confirmed by a board certified nuclear medicine physician with long experience in PET/CT reading. Salient points in the shape-encoding rendering were confirmed to designate actual lymph nodes. As it can be seen in Fig. 21, the RST-based rendering was able to correctly emphasize and color-code a lymphoma lesion, whereas a focus of comparable FDG uptake intensity in brown fat was not similarly color coded in the rendering.

5.4.4 Theoretical Reasons for Nonenhancement

During the interactive sessions with the clinicians, no lymph nodes have been identified which were not visible in the shape-encoding renderings. Theoretically, however, several reasons could prevent a filter response for the shape encoding:

1. If a lymph node has grown malignantly to such a size that it is outside of the filter size (search ray radius for RST or Gaussian kernel size for Hessian).
2. If the contrast between a lymph node and the surrounding tissue is vanishingly small.
3. If the expected spherical surface of the lymph node is deformed severely by malignant growth or extremely dense embedding in surrounding tissue of equal intensity.
4. If the noise level is so high as to render the gradient direction estimations unreliable.

6 DISCUSSION

The presented sparse radial sampling combined with the RST representation has some significant advantages which make them applicable where Hessian-based rendering does not suffice, in particular for lymph nodes and airways:

1. The gradients can be sampled at a scale space resolution which does not depend on the object size but can be chosen on a less smoothed level to optimally show the contours of the object. This is crucial for hollow objects (airways, Fig. 14) where smoothing would wipe out the thin boundary.
2. Due to the opacity accumulation along each search ray,

   a. mixing of responses from densely packed structures (e.g., vessel surrounded lymph nodes, Figs. 15, 16, 17, 18, 19, 20, and 21) is avoided,
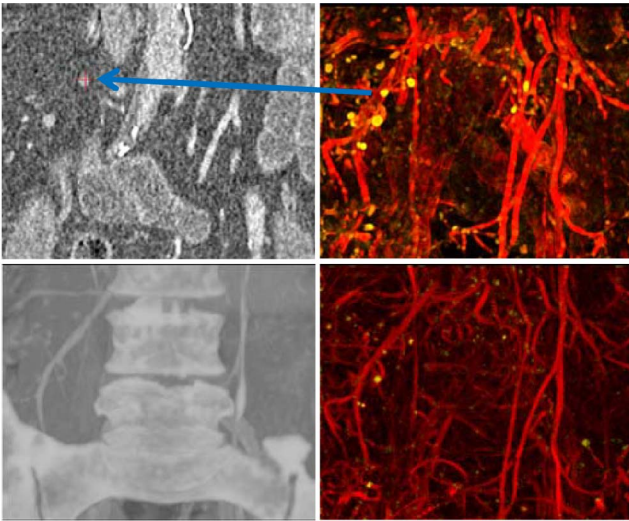
Fig. 15. Illiac lymph nodes. Upper left: axial slice view. Lower left: standard coronal MIP of the volume of interest. Upper right: coronal maximum projection rendering using the RST eigenvalues, lower right: rendering of the Hessian eigenvalues. Interviewed clinicians favored the RST-based rendering for the lymph nodes.
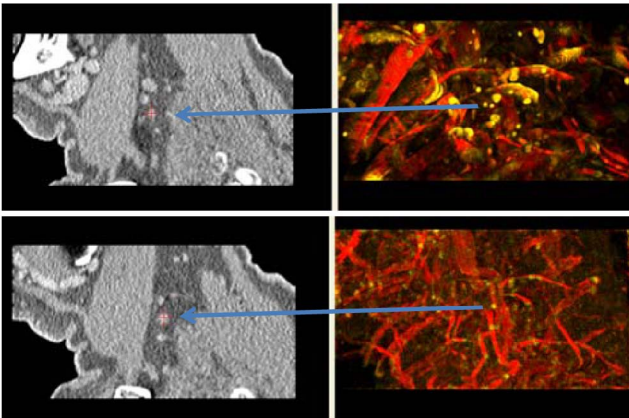

Fig. 16. Cervical lymph nodes (blue arrows, sagittal view), Hessian and RST-based approach. Left: slicewise display at two different slice positions. Right top: RST-based maximum projection rendering, bottom: Hessian-based rendering. Interviewed clinicians preferred the RST-based rendering for clearer display of the lymph nodes.

b. structures of varying sizes can be enhanced without repeated computation on varying scale space resolutions.

In comparison to the *general* structure tensor [17], [18], [19], the *radial* structure tensor representation of the
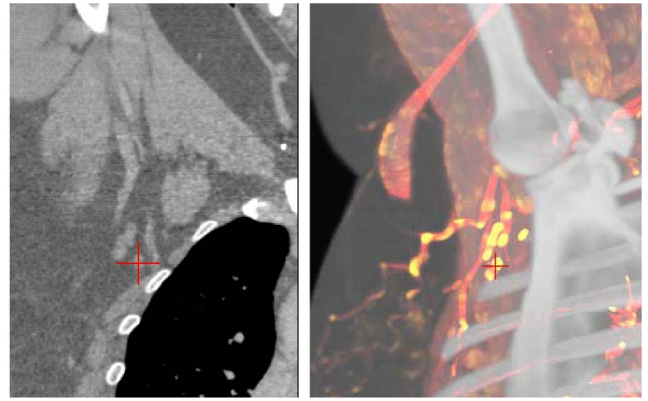

Fig. 17. Axillary lymph node. Left: standard coronal slice view. Right: RST-based rendering.
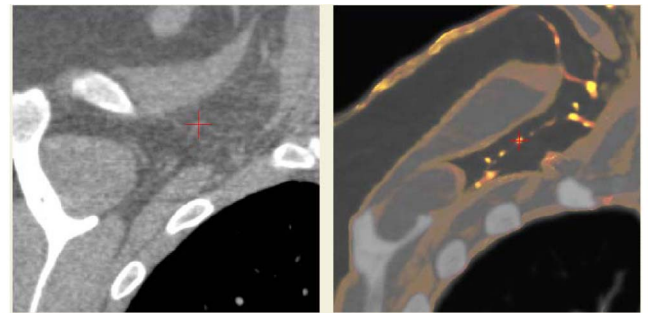

Fig. 18. A string of minuscule nodes in the axilla region barely above the noise level. Left: standard coronal slice view. Right: RST-based rendering.

neighborhood gradients is more specific to its central point, since it correlates the orientation of neighboring gradients with their relative location (Figs. 3 and 6).

Similar to direct volume rendering techniques, also the results obtained by the sparse radial sampling depend critically on an appropriate choice of the opacity transfer function (3) for a specific use case and image noise level. Extensive literature exists for the design of an optimal TF [33]. The choice of the maximum ray length is less sensitive but influences the computation time linearly. Even though sparse, the neighborhood sampling is more costly than the computation of the Hessian after prior Gaussian smoothing.

While for lymph nodes the RST approach was clearly favored by the interviewed clinicians, for vessel visualization the Hessian approach was preferred. This visual preference may cause the smoother appearance of the Hessian-based
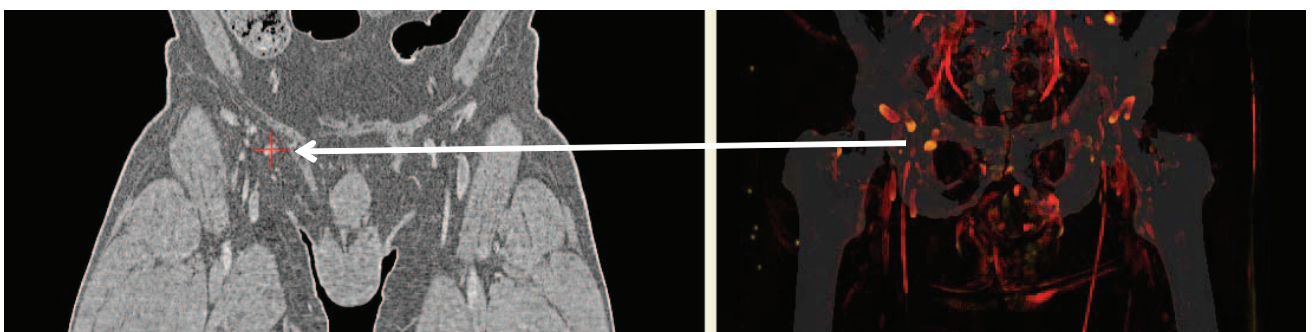

Fig. 19. Inguinal lymph nodes (coronal view). Left: slicewise display. Right: Radial structure tensor-based maximum projection rendering.
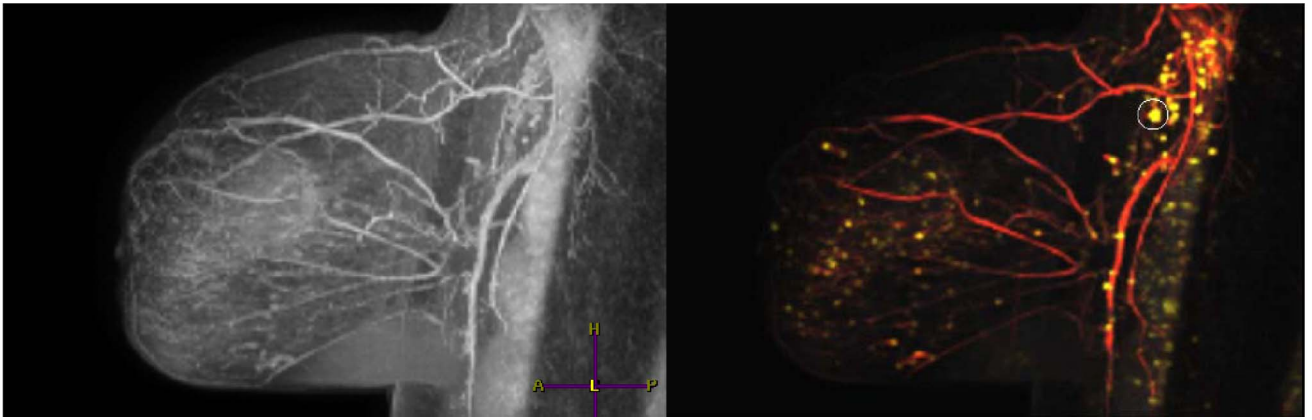
Fig. 20. Axillary lymph nodes in a breast MRI, verified by clinicians. Left: standard MIP, lymph nodes are hardly visible. Right: Hessian-based shape-encoding rendering.
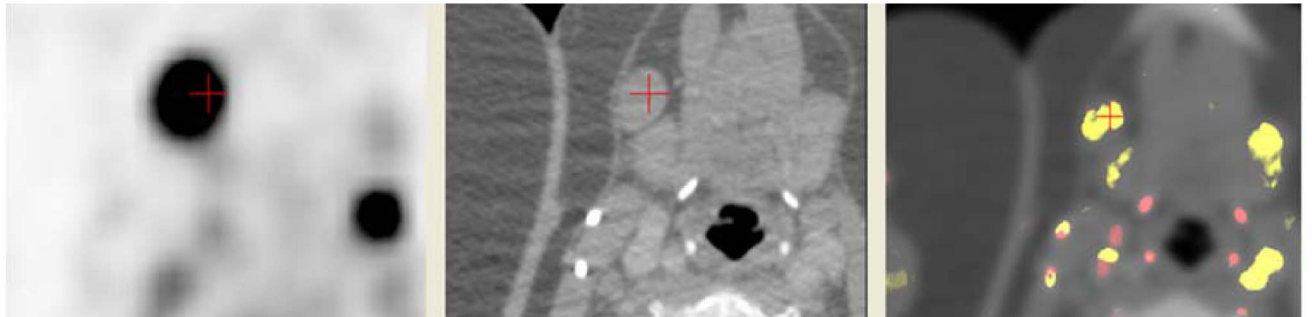

Fig. 21. Combined PET/CT scan after FDG injection, left: PET, middle: CT slice, right: slab-MIP with shape-encoding rendering, all coregistered. A lymphoma lesion close to the maxilla manifests as a FDG-hot spot (cross-hair) in the PET image (left), and is also color coded in the shape-encoding rendering (right, RST approach). The shape-encoding rendering can help to easier distinguish between hot spot stemming from spherical lymph nodes versus others stemming from brown fat.

rendering (caused by the Gaussian preprocessing) and its subtle emphasis of the centerlines (caused implicitly by stronger filter response at the object center).

Discussion with clinicians about of shape-encoding rendering often leads to comparing the underlying paradigm to fully automatic detection of anomalies by computer-aided detection and diagnosis (CADe and CADx, [45]). These algorithms typically produce explicit segmentations, object lists, and overlay markers such as circles or arrows to guide the attention. However, these distinct markers may also distract the reading physician due to their inevitable false positives. Shape-encoding rendering is an alternative concept which tries to convey useful cues in a spatial (not object-list-oriented) context, while leaving the higher level reasoning to the visual expertise of the physician.

7   CONCLUSIONS

Interviews with clinicians have shown that shape-encoding rendering can be an effective image navigation aid for certain clinical use cases, such as diagnostic inspection of nodules and lymph nodes for screening or oncological examinations. For lymph nodes in densely packed environments, derivation of the shape parameters solely from the local Hessian matrix is not always sufficient. As a complement to Hessian-based shape-encoding rendering, we present a sparse radial gradient sampling technique inspired by direct volume rendering principles, and introduce the *radial structure tensor* as an efficient

representation of the sampled gradients. The technique is computationally more costly than Hessian-based rendering, but conceptually simple and ideally suited for GPU implementation. Superior results have been shown on synthetic images and for certain clinically relevant applications such as airway and lymph node visualization.

REFERENCES

[1] C. Lundstrom, P. Ljung, and A. Ynnerman, "Local Histograms for Design of Transfer Functions in Direct Volume Rendering," *IEEE Trans. Visualization and Computer Graphics,* vol. 12, no. 6, pp. 1570-1579, Nov./Dec. 2006.
[2] D. Patel, M. Haidacher, J.P. Balabanian, and E.M. Groller, "Moment Curves," *Proc. IEEE Visualization Symp. (PacificVis' 09),* pp. 201-208, 2009.

[3] S. Lindholm, P. Ljung, C. Lundstrom, A. Persson, and A. Ynnerman, "Spatial Conditioning of Transfer Functions Using Local Material Distributions," *IEEE Trans. Visualization and Computer Graphics,* vol. 16, no. 6, pp. 1301-1310, Nov./Dec. 2010.

[4] G. Kindlmann and J.W. Durkin, "Semi-Automatic Generation of Transfer Functions for Direct Volume Rendering," *Proc. IEEE Symp. Vol. Visualization,* vol. 98, pp. 79-86, 1998.

[5] V. Pekar, R. Wiemker, and D. Hempel, "Fast Detection of Meaningful Isosurfaces for Volume Data Visualization," *Proc. IEEE Visualization Conf. (VIS '01),* p. 230, 2001.

[6] Y. Sato, C.F. Westin, A. Bhalerao, S. Nakajima, N. Shiraga, S. Tamura, and R. Kikinis, "Tissue Classification Based on 3D Local Intensity Structures for Volume Rendering," *IEEE Trans. Visualization and Computer Graphics,* vol. 6, no. 2, pp. 160-180, Apr.-June 2000.

[7] J. Hladuvka, A. König, and E. Gröller, "Curvature-Based Transfer Functions for Direct Volume Rendering," *Proc. Spring Conf. Computer Graphics,* vol. 16, pp. 58-65, 2000.

[8] G. Kindlmann, R. Whitaker, T. Tasdizen, and T. Möller, "Curvature-Based Transfer Functions for Direct Volume Rendering: Methods and Applications," *Proc. IEEE Visualization Conf. (VIS '03),* p. 67, 2003.

[9] S. Peled, H. Gudbjartsson, C.F. Westin, R. Kikinis, and F.A. Jolesz, "Magnetic Resonance Imaging Shows Orientation and Asymmetry of White Matter Fiber Tracts," *Brain Research,* vol. 780, no. 1, pp. 27-33, 1998.

[10] A. Vilanova, S. Zhang, G. Kindlmann, and D. Laidlaw, "An Introduction to Visualization of Diffusion Tensor Imaging and Its Applications," *Visualization and Processing of Tensor Fields,* J. Weickert, ed., pp. 121-153, Springer, 2006.

[11] R. Wiemker, E. Dharaiya, A. Steinberg, T. Bülow, A. Saalbach, and T. Vik, "Filter Learning and Evaluation of the Computer Aided Visualization and Analysis (CAVA) Paradigm for Pulmonary Nodules Using the LIDC-IDRI Database," *Proc. SPIE Medical Imaging,* vol. 7624, 2010.

[12] R. Wiemker, E.D. Dharaiya, and T. Bülow, "Hesse Rendering for Computer-Aided Visualization and Analysis of Anomalies at Chest CT and Breast MR Imaging," *Radiographics,* vol. 32, no. 1, pp. 289-304, Feb. 2012.

[13] H. Yoshida, Y. Masutani, P. MacEneaney, D.T. Rubin, and A.H. Dachman, "Computerized Detection of Colonic Polyps at CT Colonography on the Basis of Volumetric Features: Pilot Study," *Radiology,* vol. 222, no. 2, pp. 327-336, 2002.

[14] J.S. Praßni, J. Mensmann, T. Ropinski, and K. Hinrichs, "Shape-Based Transfer Functions for Volume Visualization," *Proc. IEEE Pacific Visualization (PacificVis '10),* pp. 9-16, 2010.

[15] T. Bülow, R. Wiemker, L. Arbash Meinel, J. Buurman, H. Abe, and G. Newstead, "Towards CAVA: Lymph Node Enhanced Visualization for Fast Visual Detection of Axillary Lymph Nodes in Breast MR Images," *Proc. Conf. Computer Assisted Radiology and Surgery (CARS '09),* 2009.

[16] H. Knutsson, "Representing Local Structure Using Tensors," *Proc. Sixth Scandinavian Conf. Image Analysis,* pp. 244-251, 1989.

[17] B. Jähne and H. Haußecker, *Computer Vision and Applications.* Academic Press, 2000.

[18] W. Förstner and E. Gülch, "A Fast Operator for Detection and Precise Location of Distinct Points, Corners and Centers of Circular Features," *Proc. ISPRS Intercommission Conf. Fast Processing of Photogrammetric Data,* pp. 281-305, 1987.

[19] J. Bigün and G.H. Granlund, "Optimal Orientation Detection of Linear Symmetry," *Proc. First Int'l Conf. Computer Vision,* pp. 433-438, 1987.

[20] T. Brox, J. Weickert, B. Burgeth, and P. Mrázek, "Nonlinear Structure Tensors," *Image and Vision Computing,* vol. 24, no. 1, pp. 41-55, 2006.

[21] S. Di Zenzo, "A Note on the Gradient of a Multi-Image," *Computer Vision, Graphics, and Image Processing,* vol. 33, no. 1, pp. 116-125, 1986.

[22] J. Bigun, T. Bigun, and K. Nilsson, "Recognition by Symmetry Derivatives and the Generalized Structure Tensor," *IEEE Trans. Pattern Analysis and Machine Intelligence,* vol. 26, no. 12, pp. 1590-1605, Dec. 2004.

[23] T. Schultz, J. Weickert, and H.-P. Seidel, "A Higher-Order Structure Tensor," *Visualization and Processing of Tensor Fields—Advances and Perspectives,* pp. 263-280, Springer, 2009.

[24] C. Xiao, M. Staring, D. Shamonin, J.H.C. Reiber, J. Stolk, and B.C. Stoel, "A Strain Energy Filter for 3D Vessel Enhancement with Application to Pulmonary CT Images," *Medical Image Analysis,* vol. 15, pp. 112-124, 2011.

[25] Q. Li, S. Sone, and K. Doi, "Selective Enhancement Filters for Nodules, Vessels, and Airway Walls in Two- and Three-Dimensional CT Scans," *Medical Physics,* vol. 30, no. 8, pp. 2040-2051, 2003.

[26] C. Lorenz, I. Carlsen, T. Buzug, C. Fassnacht, and J. Weese, "Multi-Scale Line Segmentation with Automatic Estimation of Width, Contrast and Tangential Direction in 2D and 3D Medical Images," *Proc. First Joint Conf. Computer Vision, Virtual Reality and Robotics in Medicine and Medial Robotics and Computer-Assisted Surgery,* J. Troccaz, E. Grimson, and R. Mösges, eds., pp. 233-242, 1997.

[27] A. Frangi, W. Niessen, K. Vincken, and M. Viergever, "Multiscale Vessel Enhancement Filtering," *Proc. Conf. Medical Image Computing and Computer-Assisted Intervention (MICCAI '98),* pp. 130-137, 1998.

[28] K. Krissian, G. Malandain, and N. Ayache, "Model-Based Detection of Tubular Structures in 3D Images," *Computer Vision and Image Understanding,* vol. 80, pp. 130-171, 2000.

[29] P. Mendonça, R. Bhotika, F. Zhao, and J. Miller, "Lung Nodule Detection via Bayesian Voxel Labeling," *Proc. Int'l Conf. Information Processing in Medical Imaging,* pp. 134-146, 2007.

[30] T. Pock, R. Beichel, and H. Bischof, "A Novel Robust Tube Detection Filter for 3D Centerline Extraction," *Proc. 14th Scandinavian Conf. Image Analysis (SCIA '05),* H. Kalviainen, J. Parkkinen, and A. Kaarna, eds., pp. 481-490, 2005.

[31] G. Agam, S.G. Armato, and C. Wu, "Vessel Tree Reconstruction in Thoracic CT Scans with Application to Nodule Detection," *IEEE Trans. Medical Imaging,* vol. 24, no. 4, pp. 486-499, Apr. 2005.

[32] A. Joshi, X. Qian, D.P. Dione, K.R. Bulsara, C.K. Breuer, A.J. Sinusas, and X. Papademetris, "Effective Visualization of Complex Vascular Structures Using a Non-Parametric Vessel Detection Method," *IEEE Trans. Visualization and Computer Graphics,* vol. 14, no. 6, pp. 1603-1610, Nov. 2008.

[33] X. Qian, M.P. Brennan, D.P. Dione, W.L. Dobrucki, M.P. Jackowski, C.K. Breuer, A.J. Sinusas, and X. Papademetris, "A Non-Parametric Vessel Detection Method for Complex Vascular Structures," *Medical Image Analysis,* vol. 13, no. 1, pp. 49-61, 2009.

[34] T. Lindeberg, "Scale-Space Theory: A Basic Tool for Analysing Structures at Different Scales," *J. Applied Statistics,* vol. 21, no. 2, pp. 225-270, 1994.

[35] J. Weickert, *Anisotropic Diffusion in Image Processing.* Teubner, 1998.

[36] A. Kaufman and K. Mueller, "Overview of Volume Rendering," *Visualization Handbook,* C.D. Hansen and C.R. Johnson, eds., pp. 127-174, Elsevier, 2004.

[37] D. Jones, M. Horsfield, and A. Simmons, "Optimal Strategies for Measuring Diffusion in Anisotropic Systems by Magnetic Resonance Imaging," *Magnetic Resonance Medicine,* vol. 42, pp. 515-525, 1999.

[38] C.D. Hansen and C.R. Johnson, *The Visualization Handbook.* Elsevier, 2004.

[39] P. Peloschek, J. Sailer, M. Weber, C.J. Herold, M. Prokop, and C. Schaefer-Prokop, "Pulmonary Nodules: Sensitivity of Maximum Intensity Projection versus that of Volume Rendering of 3D Multidetector CT Data," *Radiology,* vol. 243, no. 2, pp. 561-569, 2007.

[40] R. Wiemker, "Aspects of Computer-Aided Detection (CAD) and Volumetry of Pulmonary Nodules Using Multislice CT," *British J. Radiology,* vol. 78, no. suppl_1, pp. S46-S56, Jan. 2005.

[41] P.R.S. Mendonça, R. Bhotika, S.A. Sirohey, W.D. Turner, J.V. Miller, and R.S. Avila, "Model-Based Analysis of Local Shape for Lesion Detection in CT Scans," *Proc. Conf. Medical Image Computing and Computer-Assisted Intervention (MICCAI '05),* pp. 688-695, 2005.

[42] C.I. Henschke, P. Boffetta, O. Gorlova, R. Yip, J.O. DeLancey, and M. Foy, "Assessment of Lung-Cancer Mortality Reduction from CT Screening," *Lung Cancer,* vol. 71, no. 3, pp. 328-332, 2011.

[43] Y.M.T.A. van Durme, K.M.C. Verhamme, T. Stijnen, F.J.A. van Rooij, G.R. Van Pottelberge, A. Hofman, G.F. Joos, B.H.C. Stricker, and G.G. Brusselle, "Prevalence, Incidence, and Lifetime Risk for the Development of COPD in the Elderly: The Rotterdam Study," *Chest,* vol. 135, no. 2, pp. 368-377, Feb. 2009.

[44] P. Lo, B. van Ginneken, J. Reinhardt, and M. de Bruijne, "Extraction of Airways from CT (EXACT '09)," *Proc. Second Int'l Workshop Pulmonary Image Analysis,* pp. 175-189, 2009.

[45] K. Doi, "Current Status and Future Potential of Computer-Aided Diagnosis in Medical Imaging," *British J. Radiology,* vol. 78, no. suppl_1, pp. S3-S19, Jan. 2005.

Rafael Wiemker received the MS degree in astronomy from Georgia State University Atlanta in 1992, and the PhD degree in physics from the University of Hamburg, Germany in 1997. Since 1998, he has been with the Philips Research Lab Hamburg, as a senior scientist working on medical imaging topics mainly related to computer-aided detection, quantification, and visualization.

Tobias Klinder received the MS and PhD degrees both in electrical engineering from the Leibniz University Hannover, Germany, in 2006 and 2010, respectively. From 2010 to 2011, he worked at Philips Research North America on image-guided interventions. Since then, he has been with the Philips Research Lab Hamburg focusing on medical image segmentation, registration and shape modeling.

Martin Bergtholdt received the MS degree in technical engineering from the University of Mannheim, Germany, in 2002. Since 2007, he has been with the Philips Research Lab Hamburg working on medical image analysis and machine learning for clinical decision support and image-guided interventions.

Kirsten Meetz received the MS degree from the University of Heilbronn/Heidelberg and the PhD degree in medical informatics in 1996 from the German Cancer Research Center, University of Heidelberg, Germany. Since 1996, she has been with the Philips Research Lab Hamburg, as a senior scientist working on medical imaging, workflow, diagnosis and treatment decision-making topics.

Ingwer C. Carlsen received the MS degree in physics in 1977, and the PhD degree in theoretical solid-state physics in 1981 both from the Christian Albrechts University of Kiel, Germany. Since 1981, he has been with the Philips Research Lab Hamburg, as a principal scientist working on medical imaging topics and computerized clinical decision support.

Thomas Bülow received the diploma in theoretical physics in 1995 and the PhD degree in computer science in 1999 both from the Christian Albrechts University of Kiel, Germany. After postdoctoral research at the University of Pennsylvania, Philadelphia, and at the University of California, Berkeley, he joined Philips Research Hamburg in 2002, where he is working as a senior scientist on medical image segmentation, quantification, CAD, and visualization.

▷ **For more information on this or any other computing topic, please visit our Digital Library at** www.computer.org/publications/dlib.